36D.0 CHARACTERIZING ADDITIVELY MANUFACTURED INCONEL 718/738

Jeremy Shin (Mines)
Faculty: Amy Clarke (Mines)
Industrial Mentor(s): John Carpenter (LANL), Matthew Krug (AFRL)

This project was initiated in Fall 2019 and is supported by the Office of Naval Research (ONR). The research performed during this project will serve as the basis for a Ph.D. thesis program for Jeremy Shin.

36D.1 Project Overview and Industrial Relevance

This Multidisciplinary University Research Initiative (MURI) project funded by the Office of Naval Research (ONR) will focus, in part, on additively manufactured (AM) samples of Inconel 718 and Inconel 738. The goal is to analyze microstructural development, texture, and mechanical anisotropy that comes from the layer-by-layer build process, and to reveal potential variations with respect to build parameters. Experiments will be done at the Advanced Photon Source (APS) at Argonne National Laboratory (ANL) to simulate the melt pool and solidification experienced during the metal additive process. From these results, solidification behavior will be extracted and related to microstructural evolution. Sophisticated modeling software, such as FLOW-3D, will be used to more accurately determine thermal gradients based upon how the melt pool geometries change. Samples from the Manufacturing Demonstration Facility (MDF) at Oak Ridge National Laboratory (ORNL) will also be characterized to clarify the role of scan strategy on resulting microstructural and mechanical anisotropy. This work is of interest to the aerospace sector, as Ni-based superalloys are desirable for their creep behavior and oxidation resistance, making them excellent candidates for gas turbines and other internal propulsion parts. Inconel 718 and 738 are already heavily used alloys for these applications, and understanding the differences between the microstructures produced by AM and conventional methods will lead to the manufacturing of improved parts with controlled microstructures and properties.

Ni-based superalloys are commonly used in aerospace applications for their high-temperature properties, and current alloy design focuses on AM to produce parts with complex geometries and near-net shapes through a layer-by-layer process [36D.1]. The aim of AM parts is to eliminate processing steps to save resources and costs for production. The microstructural evolution of printed parts is poorly defined, as thermal cycling and large thermal gradients from the build process differ from legacy manufacturing techniques such as casting and forging. Common techniques for metallic AM include selective laser sintering (SLS), selective laser melting (SLM), and electron beam melting (EBM). These processes can introduce defects such as voids and lack of fusion between printed layers, which negatively affect mechanical and fatigue properties [36D.2]. **Figure 36D.1** shows the variation of structure and properties along the build direction for an AM build of a Ni-based superalloy made with EBM and powder feedstock [36D.3]. It is important to understand fundamental materials science phenomena through *in-situ* and *ex-situ* experiments to better understand the end-result microstructures and material properties. The *in-situ* experiments will consist of simulating the melt pool and solidification during a typical AM build process using the APS facilities, while *ex-situ* experiments will consist of electron microscopy, including electron backscatter diffraction (EBSD), and neutron diffraction to understand microstructural condition as a function of build height.

36D.2 Previous Work

As the MURI project was initiated in Fall 2018, experiments similar to the scope of this project were conducted a year ago at the APS in March 2019 with model ternary Ni-alloys and Inconel 738. The model alloys used were single-crystal specimens with differing Ni, Mo, and Al contents evaluated at different laser powers. The R2 samples (Ni-1.9Mo-6.6Al (wt %)) had either a ⟨110⟩ or ⟨111⟩ orientation parallel to the build direction, while the R4 samples (Ni-22.2Mo-2.8Al (wt %)) had either a ⟨100⟩ or ⟨110⟩ orientation parallel to the build direction. The radiography data was processed using an ImageJ script to minimize background noise and to more clearly track the solid-liquid interface. Solidification velocities were determined at different power settings and compared with post-mortem electron microscopy to analyze the role of laser power on the columnar to equiaxed transition (CET) [36D.4].

The EBM Inconel 738 samples made at the MDF focused on relating the scan strategy of the build to the degree of texture along the build direction. The EBM samples were made with three scan strategies: Random, Linear, and DeHoff methods. The Random method spot melts the powder in random locations until the layer is completely melted.

The Linear method raster melts the powder material from edge to edge in a straight path with a rotation experienced between layers, while the DeHoff method is more complicated by spot melting powder material every 11th voxel until layer completion. Only the Random and Linear samples have been manufactured, while the other sample with DeHoff scan strategy is to be delivered in the future from the MDF [36D.5].

36D.3 Recent Progress

36D.3.1 Experiments at the APS

Beamtime at Sector 32-ID at the APS was allocated in February 2020 to observe real-time solidification dynamics using synchrotron X-ray imaging. Experiments were performed at low, medium, and high laser powers to sample a large portion of G-V space, where G is the thermal gradient and V is the solidification front velocity. Equiaxed grain Inconel 718 specimens, provided by MURI collaborators from the University of California Santa Barbara, were tested with and without a powder layer to observe any possible differences in the CET caused by the powder layer. Inoculated Inconel 718 as-built samples, provided by Elementum 3D, were tested with an inoculated powder layer to determine effects on the CET. Inconel 738 samples were tested with and without a powder layer as well. Interestingly, hot cracking was observed in the Inconel 738 samples with *in-situ* radiography in higher laser power conditions. All samples were tested with both spot melt and raster scan conditions. Other inoculated Ni-alloys (provided by Elementum 3D) were tested, including Inconel 625, Hastelloy 276, Rene 80, and CM 247LC. A few of these alloy samples showed severe keyholing phenomena and void formation. This was probably related to the thin geometry of these samples, necessitated by their densities and the need for thin sample geometries to achieve x-ray transmission.

36D.3.2 Top-down Imaging of Melt Pools (Inconel 738)

Before EBSD evaluation of tested APS samples, there needs to be preliminary analysis of the melt pool surfaces, as this information will be lost upon sample mounting and cross-section polishing. All Inconel 738 spot and raster scans were observed in an SEM to identify interesting melt pool features and potential cracking events. **Figure 36D.2** includes an image of a typical spot melt, whereas **Figure 36D.3** includes an image of a typical raster scan. Both figures at low magnification use secondary electrons. Higher magnification images use back-scattered electrons to create channeling contrast, revealing fine features. The summary of all spot and raster scan melt conditions is included in **Table 36D.1** and **Table 36D.2**, respectively, for the Inconel 738.

With increasing power density, the surface of the spot melt shows a centerline between the two solidification fronts. This may be indicative of cracking, but it is more likely an artifact of the thin sample geometry and the volume of liquid spreading out that causes shrinkage in the end region. **Figure 36D.4** shows a series of increasing power density spot melts to better illustrate the centerline that becomes more pronounced at higher power densities. The opposing dendrite orientations at the centerline support the theory that this interface is a result of solidification boundaries on the thin-wall geometry. There are no visible cracks on the surface and melt pool shapes are of little interest.

The raster scan specimens actually show several cracking defects on the surface. There is no centerline issue, as the heat source is no longer stationary, moving linearly in one direction, and solidification follows in one direction on the surface of the sample. **Figure 36D.5** shows several examples of surface cracks that are several microns in length, although not all samples had cracks. This data shows that there are conditions for which cracks do and do not form upon solidification. Determinations of thermal gradients (G) and solidification velocities (V) still need to be conducted to identify where the samples lie in G-V space. The G values will need to use a simulation software known as FLOW-3D to account for the complex shape evolution of the melt pool. The V values will be found using the in-situ radiography data and tracking the solid-liquid interface as a function of time and distance. This will be compared with cracking events found in the SEM to understand which conditions lead to hot cracking. In order to determine the cracking internally, a cross-section of the specimen will be needed. Consideration will be given for how to section the sample, as an internal crack may not run through the entirety of the specimen.

36D.3.3 Planning for Neutron Diffraction Experiments at LANL

Samples of varying geometries of Haynes 282 were provided by ORNL, including a pyramid structure and two rectangular structures with differently shaped internal gaps. **Figure 36D.6** shows a schematic of these samples and

the internal geometry. The purpose of these specimens is to investigate how the very different geometries and the related local thermal gradients affect the microstructure in that region. A sample of inoculated Inconel 718 was provided by Elementum 3D. This specimen will be analyzed using the same neutron diffraction technique to see the effect of inoculant particles on the underlying microstructure.

36D.4 Plans for Next Reporting Period

All samples from the previous APS run will undergo post-mortem microstructural analysis, including:

- EBSD on spot and raster melts of Inconel 718 and Inconel 738 to determine the effects of varying laser power densities on grain size and morphology.
- Define a hot-cracking regime for Inconel 738 under LPBF conditions using solidification velocity profiles from *in-situ* radiography data and post-mortem electron microscopy; FLOW-3D simulation software will be used to more accurately account for the complex melt pool shape in order to find thermal gradients.
- Neutron diffraction measurements on IN718 inoculated samples at Los Alamos National Laboratory to analyze texture and differences in properties along the build height.
- Neutron diffraction measurements on Haynes 282 (different geometries) at Los Alamos National Laboratory to relate local differences in thermal gradients to microstructure development; similar experiments are also to be done on other MDF samples including Raster scan strategy builds of IN738.

36D.5 References

[36D.1] T.M. Pollock, Alloy design for aircraft engines, Nat. Mater. 15 (2016) 809–815.

[36D.2] W.E. Frazier, Metal additive manufacturing: A review, J. Mater. Eng. Perform. 23 (2014) 1917–1928.

[36D.3] S.S. Babu, N. Raghavan, J. Raplee, S.J. Foster, C. Frederick, M. Haines, R. Dinwiddie, M.K. Kirka, A. Plotkowski, Y. Lee, R.R. Dehoff, Additive Manufacturing of Nickel Superalloys: Opportunities for Innovation and Challenges Related to Qualification, Metall. Mater. Trans. A Phys. Metall. Mater. Sci. 49 (2018) 3764–3780.

[36D.4] J. Klemm-Toole, A. Clarke, Combining in-situ and ex-situ characterization to understand crystallographic texture development in metal additive manufacturing, CANFSA Report, Project 36C, Oct. 2, 2019.

[36D.5] A. Saville, A. Clarke, Rationalization of liquid/solid and solid/solid interface instabilities during thermal-mechanical transients of metal additive manufacturing, CANFSA Report, Project 36A, Mar. 27, 2019.

36D.6 Figures and Tables

Table 36D.1: Processing conditions for spot melts of Inconel 738.

Material	Laser Power (% of Total)	Effective Power (W)
IN738	10	24.9
IN738	20	82.1
IN738	30	139.4
IN738	40	196.6
IN738	50	253.8
IN738	60	311.1
IN738	70	368.3
IN738 w/powder	10	24.9
IN738 w/powder	20	82.1
IN738 w/powder	30	139.4
IN738 w/powder	40	196.6
IN738 w/powder	50	253.8
IN738 w/powder	60	311.1
IN738 w/powder	20	82.1

Table 36D.2: Processing conditions for raster scans of Inconel 738.

Material	Laser Power %	Effective Power (W)	Laser Speed (m/s)
IN738	40	196.6	0.5
IN738	30	139.4	0.5
IN738	35	168.0	0.5
IN738	20	82.1	0.25
IN738	90	482.8	2
IN738 w/powder	35	168.0	0.5
IN738 w/powder	40	196.6	0.5
IN738 w/powder	20	82.1	0.25
IN738 w/powder	90	482.8	2
IN738 w/powder	90	482.8	1.5

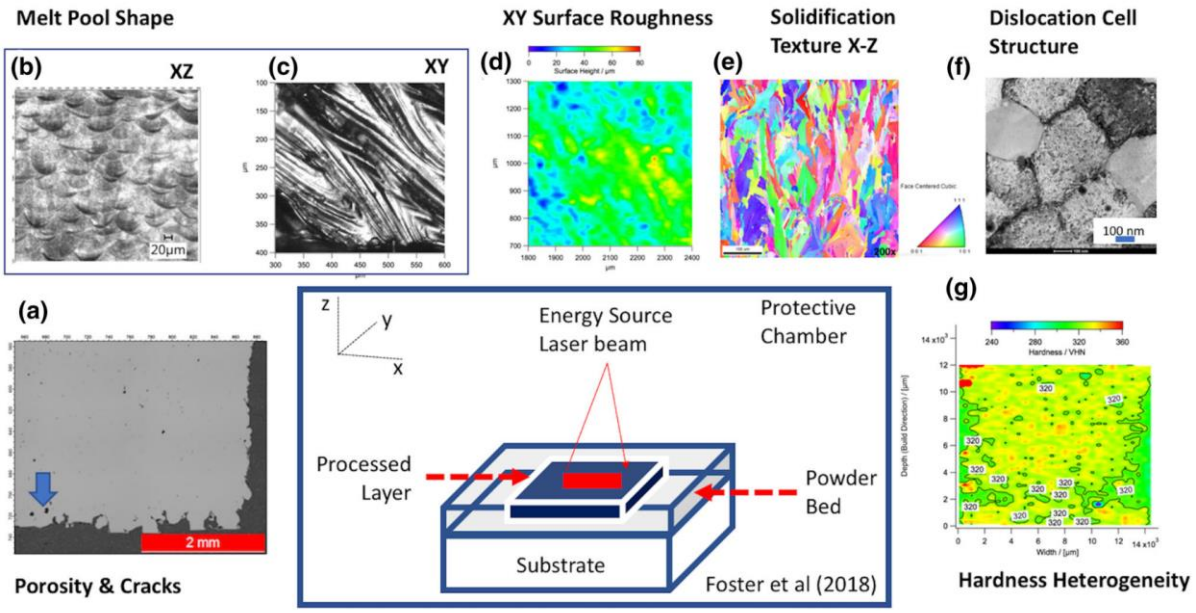

Figure 36D.1: Key features and characteristic microstructures for an AM build of a Ni-based superalloy [36D.3].

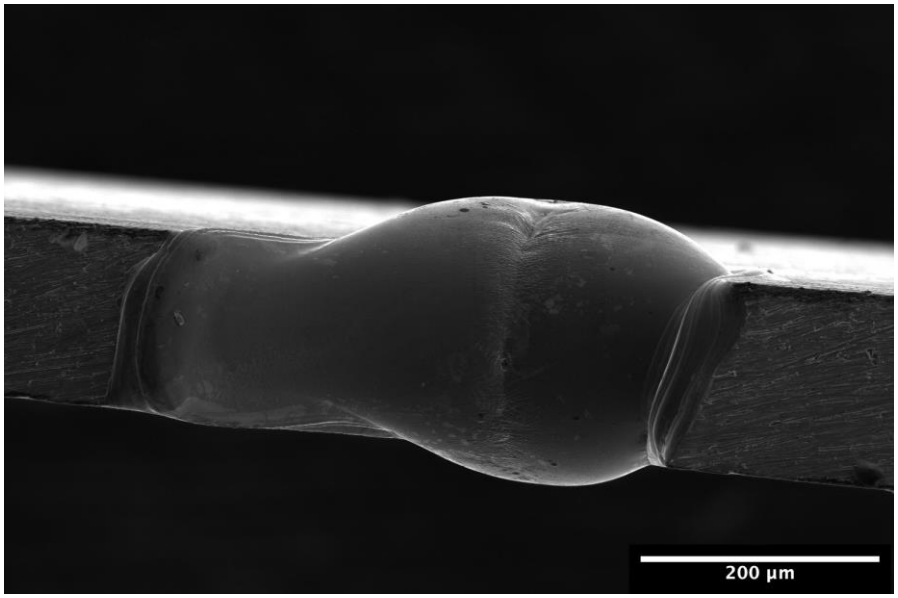

Figure 36D.2: SEM image of a spot melt, surface of melt pool, at 368.4W (high) power setting.

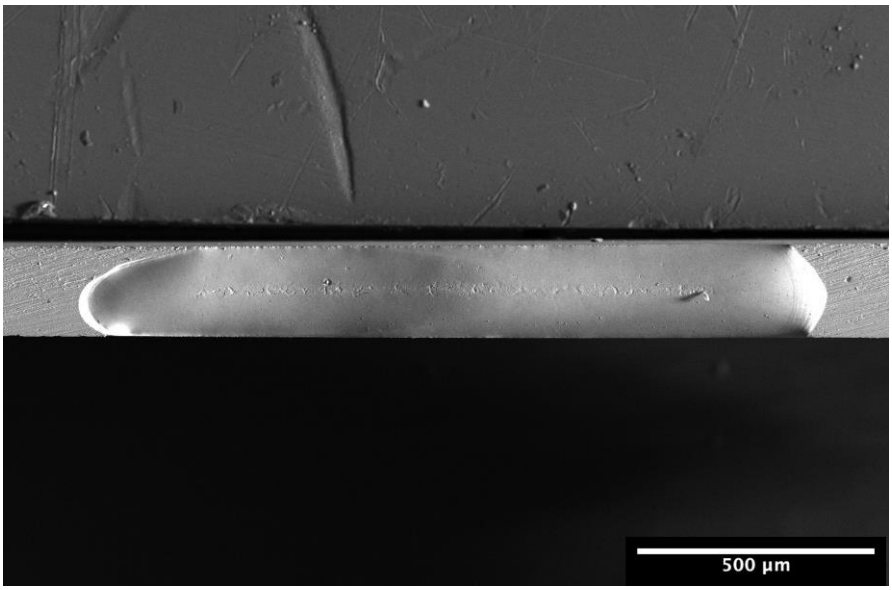

Figure 36D.3: SEM image of a raster scan, surface of melt pool, at 168.0W (medium) power setting.

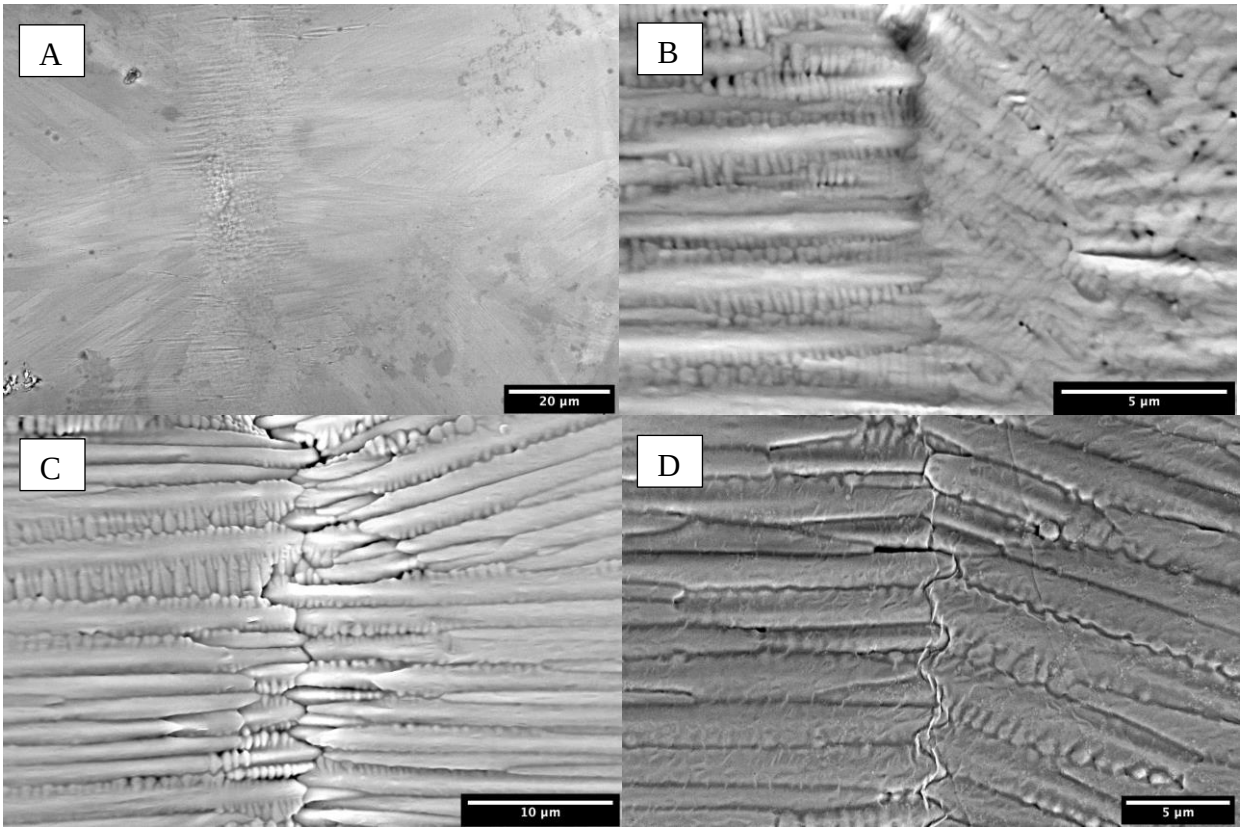

Figure 36D.4: The solidification centerline becomes more pronounced as the power density is increased. The power densities for each figure are A – 82.1W (20%), B – 139.4W (30%), C – 253.8W (50%), D – 311.1W (60%). These images are all taken with backscattered electrons.

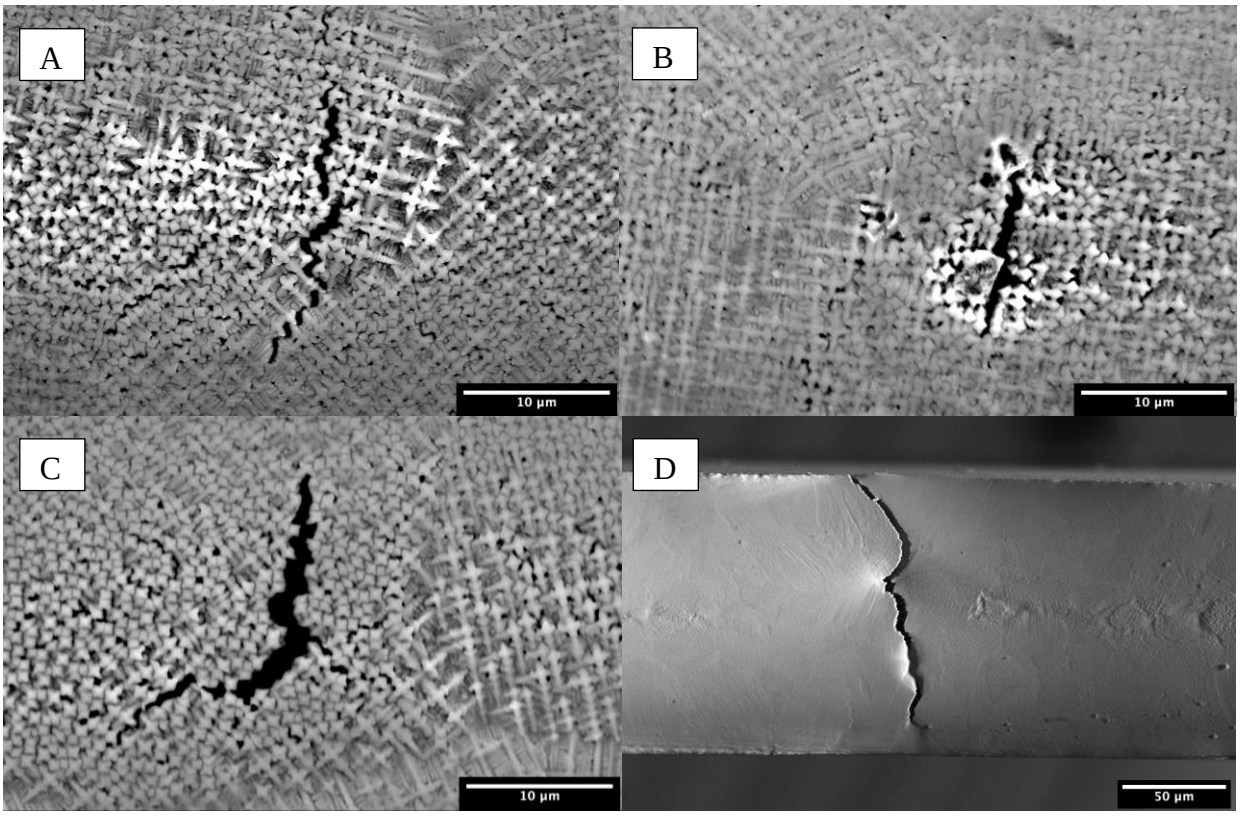

Figure 36D.5: Examples of cracks in different raster scans of the Inconel 738. The power densities for each figure are A – 82.1W (20%), B – 239.4W (30%), C – 168.0W (35%), D – 482.8W (90%). These images are all taken with backscattered electrons. Images are taken throughout the length of the raster scan.

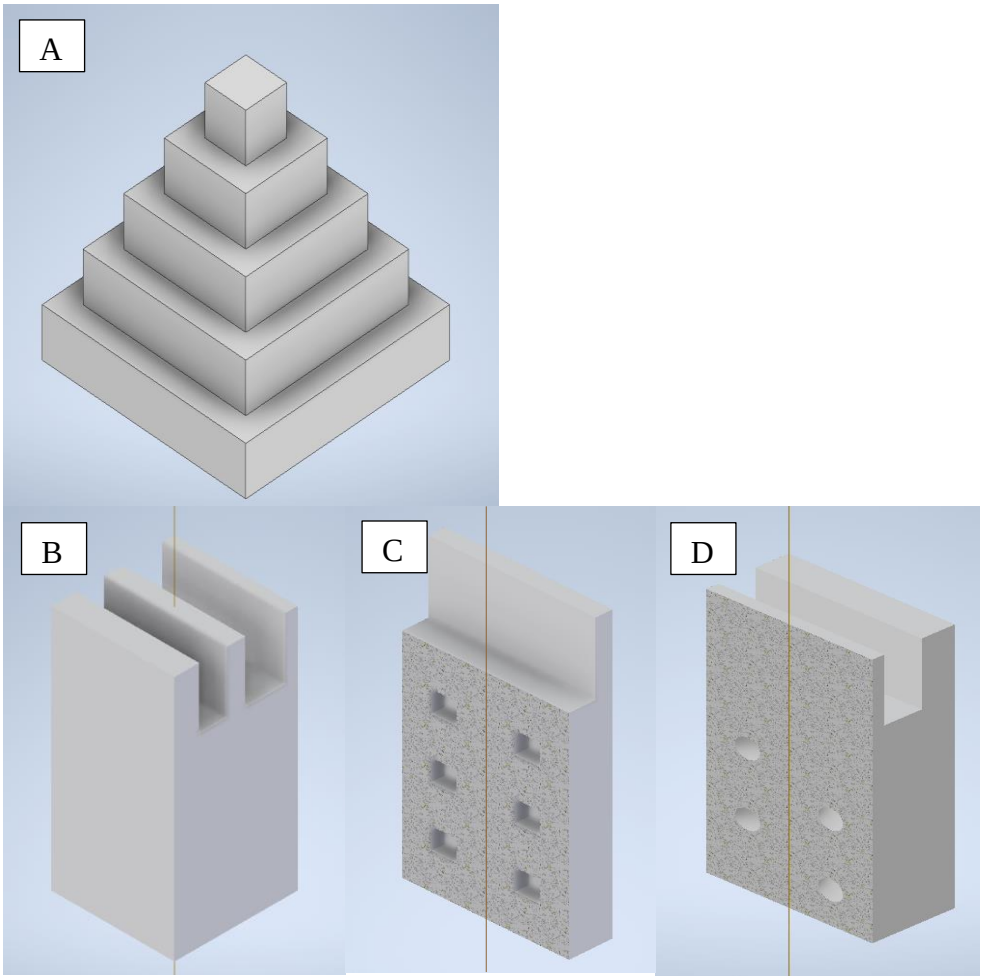

Figure 36D.6: A shows a pyramid geometry with a 25 x 25 mm base and 5 x 5 mm step size. Figure B shows the rectangular sample with a 20 x 20 x 30 mm body and 2/3/4mm struts on top. Figures C and D show the different gaps inside of the rectangular sample with 3 x 3 mm cubes and 3mm diameter spiral, respectively.